OPTIma

Winter, Alasdair; Aitkenhead, A.; Allinson, N.; Allport, P.; Esposito, M.; Green, S.; Kirkby, K.J.; MacKay, R.I.; Manger, S.; Merchant, M.J.; Price, T.; Pyatt, S.; Taylor, M.J.; Waltham, C.

DOI:
10.1088/1748-0221/18/04/p04026

Jinst

Published by IOP Publishing for Sissa Medialab

Received: *January 19, 2023*
Revised: *March 17, 2023*
Accepted: *March 22, 2023*
Published: *April 19, 2023*

OPTIma: a tracking solution for proton computed tomography in high proton flux environments

A. Winter,[a,c,*] **A. Aitkenhead,**[d,e] **N. Allinson,**[c] **P. Allport,**[a] **M. Esposito,**[c] **S. Green,**[b] **K.J. Kirkby,**[d,e] **R.I. MacKay,**[d] **S. Manger,**[d,e] **M.J. Merchant,**[d,e] **T. Price,**[a] **S. Pyatt,**[a] **M.J. Taylor**[d,e] **and C. Waltham**[c]

[a] *University of Birmingham, Birmingham, United Kingdom*
[b] *Department of Medical Physics, University Hospitals Birmingham NHS Trust, Birmingham, United Kingdom*
[c] *University of Lincoln, Lincoln, United Kingdom*
[d] *The Christie NHS Foundation Trust, Manchester, United Kingdom*
[e] *University of Manchester, Manchester, United Kingdom*

E-mail: alasdair.winter@cern.ch

Abstract: Currently there is a large discrepancy between the currents that are used for treatments in proton beam therapy facilities and the ultra low beam currents required for many proton CT imaging systems. Here we provide details of the OPTIma silicon strip based tracking system, which has been designed for performing proton CT imaging in conditions closer to the high proton flux environments of modern spot scanning treatment facilities. Details on the physical design, sensor testing, modelling, and track reconstruction are provided along with Monte-Carlo simulation studies of the expected performance for proton beam currents of up to 50 pA at the nozzle when using a $\sigma =\sim 10$ mm spot scanning cyclotron system. Using a detailed simulation of the proposed OPTIma system, a discrepancy of less than 1% on the Relative Stopping Power is found for various tissues when embedded within a 150 mm diameter Perspex sphere. It is found that by accepting up to 7 protons per bunch it is possible to operate at cyclotron beam currents up to 5 times higher than would be possible with a single proton based readout, significantly reducing the total beam time required to produce an image, while also reducing the discrepancy between the beam currents required for treatment and those used for proton CT.

Keywords: Instrumentation for hadron therapy; Si microstrip and pad detectors; Detector modelling and simulations I (interaction of radiation with matter, interaction of photons with matter, interaction of hadrons with matter, etc); Particle tracking detectors

*Corresponding author.

https://doi.org/10.1088/1748-0221/18/04/P04026

2023 JINST 18 P04026

Contents

2023 JINST 18 P04026

1 Introduction

Proton radiotherapy is an alternative to conventional X-ray radiotherapy that aims to improve the ratio of dose delivered to the target site relative to that received by neighbouring healthy tissue. This potential improvement arises from the characteristic Bragg peak in the depth-dose profiles of hadrons, however this profile also introduces new challenges for treatment planning. Due to the sharp drop off in dose at the end of the proton range it is essential that an accurate image of the Relative Stopping Power (RSP) throughout the patient is available to ensure that the location of the dose can be accurately predicted. Current treatment planning is based on kilovoltage X-ray CT, and the resulting image is converted from Hounsfield units to RSP. This conversion introduces an uncertainty into the resulting estimate of the RSP. The total estimated uncertainty on the RSP from performing Dual Energy CT is found to be $\sim$ 1–3% [1, 2] depending on the tissues involved. Proton Computed Tomography (pCT) [3] offers a way to reduce these uncertainties by imaging the patient directly with protons, allowing for direct measurement of the RSP.

Because of Multiple Coulomb Scattering (MCS) it has been recognised that simply integrating protons to produce an image would result in poor quality imagery, and that the tracks of individual protons must be recorded [4]. As such, pCT systems typically consist of detectors capable of tracking

the trajectory of a proton as it enters and exits the patient, followed by a device for estimating the energy lost by the proton along this trajectory. Further to performing a pCT for treatment planning, such a setup can in principle provide the necessary tools for patient alignment, beam range verification and daily plan adaption using the proton beam itself.

Several prototype systems have been built to perform pCT, however typically these have been designed to deal with low fluxes corresponding to only a single proton in the measurement system at any one time (for a recent review see for example [5]). Minimum cyclotron treatment currents are typically $O(200\,\text{pA})$ at the nozzle and are delivered in pulses at frequencies of $O(100\,\text{MHz})$ corresponding to $O(10)$ protons per bunch [6, 7]. As such there is currently a large discrepancy between the beam conditions required for pCT vs those used for treatment. Any system that only accepts a single proton per bunch will only be able to use a small fraction of the bunches being delivered by the cyclotron. As such, this type of system would inherently have a very low efficiency which results in longer scan times and a considerable amount of wasted dose delivered to the patient in order to acquire the necessary number of usable protons (see section 2.3).

Optimising Proton Therapy through Imaging (OPTIma) has been designed to overcome these problems by operating at higher proton fluxes of up to (currently) 7 protons per bunch and thus requires less dose to the patient and provides shorter scan times. The system will be tested on the research beamline of the cyclotron at The NHS Christie Proton Beam Therapy Centre, Manchester [8] which uses a Varian (Palo Alto, CA, U.S.A.) ProBeam cyclotron-based spot scanning system with minimum operating currents of$\sim 250\,\text{pA}$ (at 200 MeV) delivered at a pulse rate of 72 MHz, and can produce spots of up to $\sigma = \sim 10\,\text{mm}$. In order to achieve the lower currents studied here, the system design includes an additional collimator upstream of the scanning system in the research beamline.

Here we focus on the tracking component of the system and the expected performance as a function of beam current. In section 2 we discuss the physical layout of the tracking system along with the current status of the testing/assembly. The simulation model of the trackers and the track reconstruction procedure are covered in sections 3 & 4. The expected performance of the system for various beam currents is shown in section 5 and discussed more broadly in section 6. Subsequent papers will discuss the custom read-out ASIC, the calorimeter and the DAQ's digital architecture in detail.

2 The OPTIma system

OPTIma was developed as a follow on to the PRaVDA [9] project which was designed for operating with broad passively scattered beams, with the aim of developing a system that is appropriate for modern clinical facilities which operate using scanned pencil beams and higher beam currents [6, 7]. The overall tracker design is shown in figure 1. Each proton trajectory is reconstructed using four silicon strip based tracking modules, with two in front of the patient and two after to record the incoming and outgoing trajectory. Each module is made up of 2–4 layers of silicon strips with an active area of $\sim 60 \times 360\,\text{mm}^2$ per layer. The tracking system is then followed by a segmented scintillator based calorimeter to measure the residual energy of the protons. The full system is designed such that it can be translated to cover a full scan area of $\sim 360 \times 360\,\text{mm}^2$.

2023 JINST 18 P04026

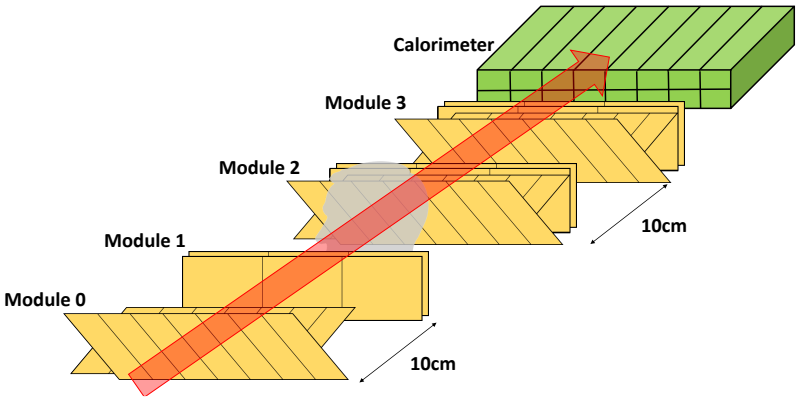

Figure 1. The overall design of the OPTIma system consisting of 12 layers of silicon strips distributed across 4 tracking modules followed by a calorimeter. Each pair of modules is separated by 10 cm while the gap between modules 1 and 2 is adjusted depending on the phantom size.

2.1 Sensor design

The sensors used for the trackers are based on those designed for the ATLAS ITk system [10] which uses n-on-p type silicon strips for increased radiation hardness and were supplied by Hamamatsu Photonics U.K. Here the sensor thickness is reduced to 150 µm to minimise the amount of material in the beam and thus reduce the energy loss and scattering of the protons within the detectors. Silicon strips provide a relatively cheap, robust, radiation hard tracking solution that can be read out at frequencies matching the high bunch repetition rates of clinical cyclotrons.

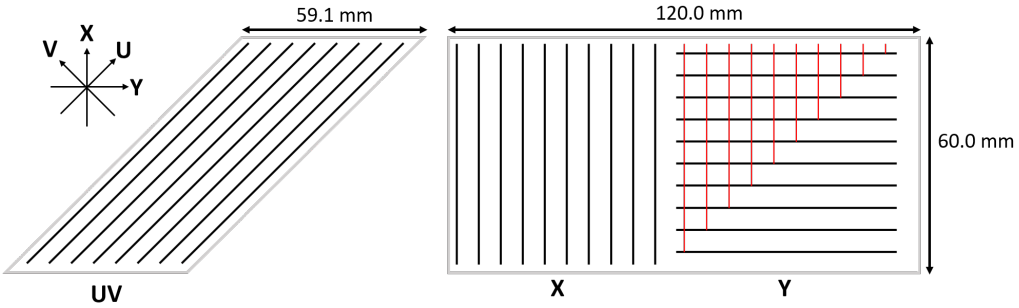

Figure 2. A schematic view of a UV (left) and XY (right) silicon strip sensor. The strip orientations are shown in black. An additional layer of metal (red) is included on the Y section to route the signal to the top edge of the device from which readout will occur.

In total it was determined that four different strip orientations were necessary to allow for suitable track reconstruction. To provide these different orientations, two different sensor variants have been developed (see figure 2). In both cases the height of the sensor (60 mm) is determined by the maximum expected spot size at The Christie's research line after the beam has travelled through 22 cm of water, roughly equivalent to the depth of a typical human head.

The first variant is the UV sensor which provides segmentation in the ±45° directions depending on how the sensor is oriented. Each UV sensor is a parallelogram of width 59.1 mm, height 60.0 mm containing 256 strips of pitch 159 µm . A total of 6 UV sensors are required to cover a 36 cm wide area.

2023 JINST 18 P04026

The second variant is the XY sensor which provides segmentation in the 0° and 90° directions. Each XY sensor is a $6 \times 12\,\mathrm{cm}^2$ rectangle that is divided into two halves. The left half, 'X', contains 256 strips segmented in the horizontal direction, while the right half, 'Y', contains 252 strips segmented in the vertical direction. In both sections the strip pitch is 232 µm . As 3 XY sensors must be tiled to provide the intended coverage of 360 mm, an additional metal layer is added to the 'Y' section to redirect the signal output to the long edge of the sensor so that no deadspace is required for readout on the tiled edges. Two separate $6 \times 6\,\mathrm{cm}^2$ devices could have been used for the X and Y orientations, however by including both orientations on a single sensor it reduces the number of devices that need to be tiled and thus reduces the number of gaps within the layer. In principle, separate $6\mathrm{x}12\,\mathrm{cm}^2$ devices could also have been used for the X and the Y strips, however such an option would require separate wafer designs for the X and Y variants which introduces additional cost with no notable benefit over the combined solution.

2.2 Module layout

As each layer of silicon provides only a 1 dimensional positional measurement, it is necessary to combine multiple layers with different orientations into a module such that a proton's (x, y) coordinate can be reconstructed from the combined information provided. In order to minimize the uncertainty on these (x, y) coordinates, the modules have been designed to minimize the separation between the various silicon layers such that each one dimensional measurement is taken at approximately the same z-position.

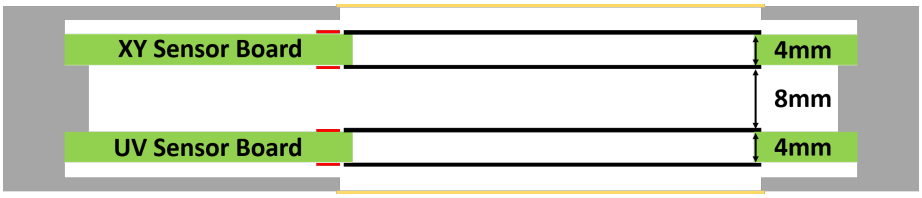

Figure 3. Layout of one of the rear tracking modules showing the 4 layers of silicon (black) arranged on 2 sensor boards. The support structure (grey) is left open across the active area to minimise material in the beam, though a thin layer of Mylar (yellow) is used to protect the sensors from the environment. Readout is carried out along one edge of the sensors using a set of ASICs (red).

The layout of a module is shown in figure 3. Each module houses up to 2 sensor boards, with each sensor board being a single PCB instrumented with silicon on both sides. An XY sensor board is instrumented with XY sensors on each side where the sensors on one side have been flipped in such a way that the X part of a sensor on one side lines up with the Y part on the other. The UV board is similar in that it is instrumented with UV sensors on either side with the 2 sides orientated in such a way that the 2 sets of strips are orthogonal.

As each sensor board has 2 layers of orthogonal strips on it, either sensor board is capable of providing an (x, y) coordinate on its own. When dealing with single proton bunches this would be sufficient, however when multiple protons enter the system at once, ambiguities arise and the second sensor board provides disambiguation by providing two additional axes of measurement.

A total of four modules are required to reconstruct the full trajectory of each proton. The modules are arranged into two mini-trackers, each consisting of a pair of modules separated by

2023 JINST 18 P04026

10 cm, with one mini-tracker providing the incoming trajectory and the other the outgoing. The gap between the two mini-trackers is adjusted based on the size of phantom being imaged with the aim of minimising any extrapolation of the proton path from the trackers to the phantom.

In the case of the incoming trajectory it was found that a single sensor board was sufficient for each module as the knowledge of the beam origin can provide suitable disambiguation. As a result the front module only contains a UV sensor board while the second only contains an XY sensor board. This technique of using the beam origin as a third tracking point is not viable for the rear trackers as there can be too much scattering of the beam within the phantom and so both sensor board types are included per module.

In total this gives 12 silicon layers (1.8 mm) in the beam. This is the same number of layers as was used by PRaVDA however due to the more compact modules and optimized layer distribution, an improved performance is anticipated.

2.3 Readout

A full description of the custom read-out ASIC and the DAQ's digital architecture will be provided in subsequent papers, however the expected limitations on the system are discussed here.

It is anticipated that due to bandwidth limitations from the DAQ it will be necessary to limit the maximum number of protons per bunch to 7 in the readout. Any readout cycles that report 8 or more hits in any layer of the detector will be rejected at hardware level. This upper limit on the number of protons introduces an additional inefficiency in the system which will be dependent on the pulse frequency and beam current.

Using the Christie's 72 MHz cyclotron as a typical example and assuming Poisson statistics, tables 1 & 2 show the distribution of the number of protons per bunch for the minimum and maximum currents studied here, and the efficiency of a pCT system as a function of the number of protons it can read out when accounting for the weighting of bunches i.e. a bunch carrying N protons will deliver N times the dose.

It can be seen that at 50 pA the impact of accepting up to 7 protons is an efficiency of 85%. This figure should be compared against accepting single protons, which would yield an efficiency

Table 1. Expected distribution of the number of protons per bunch for a 10 and 50 pA beam (at the nozzle) with a 72 MHz pulse rate.

Protons Per Bunch	Probability at 10 pA	Probability at 50 pA
0	0.42	0.01
1	0.36	0.06
2	0.16	0.12
3	0.05	0.18
4	0.01	0.19
5	< 0.01	0.17
6	< 0.01	0.12
7	< 0.01	0.07
8	< 0.01	0.04

2023 JINST 18 P04026

Table 2. Efficiency of the system as a function of the maximum number of protons it can accept, N, for a 10 and 50 pA beam (at the nozzle) with a 72 MHz pulse rate.

N	Efficiency at 10 pA (%)	Efficiency at 50 pA (%)
0	0.0	0.0
1	42.0	1.3
2	78.5	7.0
3	94.2	19.3
4	98.8	37.1
5	99.8	56.4
6	> 99.9	73.1
7	> 99.9	85.2
8	> 99.9	92.6

of just 1.3% at 50 pA or 42.0% at 10 pA. As such, it is unlikely that a single proton system would be operated at currents higher than 10 pA due to the resulting low dose efficiency. Operating at lower currents than 10 pA would improve the single proton efficiency and thus reduce the required dose, however this could potentially lead to long scan times. For the total dose considered in section 5 (approximately 3×10^9 protons), the total beam time required to acquire this dose when accepting up to 7 protons per bunch at 50 pA is 11 s, while operating at 10 pA and only accepting single protons would require 114 s. In practice there will also be unavoidable factors which contribute to the total imaging time such as patient setup and finite gantry rotation speeds which typically add up to at least 5 minutes. As such, operating at 50 pA ensures that the beam time is a negligible component of the total imaging time, while operating at < 10 pA may lead to the beam time becoming a limiting factor.

Further, while some facilities can achieve beam currents below 10 pA by introducing collimators or defocusing the beam, it is also not always trivial to make such changes when operating on a clinical treatment line where patients are involved. At the Christie facility the minimum beam current supplied by the Varian commercial system is $\sim$ 250 pA. As such, 10 pA can only be achieved by adding a collimator to reduce the current by a factor of 25. This collimator will be added to the research line but would not be permitted on any of the treatment lines due to the potential impact on clinical work flow and patient safety. In future, commercial systems may choose to expand their operating conditions to supply lower beam currents for pCT, but currently it is not possible to guarantee the beam currents required for single proton imaging in all treatment facilities. Even operating at 50 pA, OPTIma still only represents a step towards operating at clinical treatment facilities but is not quite the full solution as it still requires a factor of 5 reduction in the cyclotron beam current.

Due to the limitation on the number of hits per readout cycle, it is essential that only valid hits are recorded to avoid saturating the system. Additional hits can be generated either by charge sharing or by noise. Charge sharing occurs when a proton hits the system near the boundary of two adjacent strips and generates sufficient charge that both strips go above the system threshold. Such cases are expected to occur at a rate of $\sim$1% and are dealt with at hardware level by only reporting the first hit if two adjacent hits are recorded. Noise is not anticipated to be a significant issue as the expected signal size (most probable value of 25,000 e) is sufficiently large that a suitably chosen threshold of 10,000 e is expected to reject noise at a 5σ level with minimal loss of efficiency.

2023 JINST 18 P04026

2.4 Sensor testing & assembly

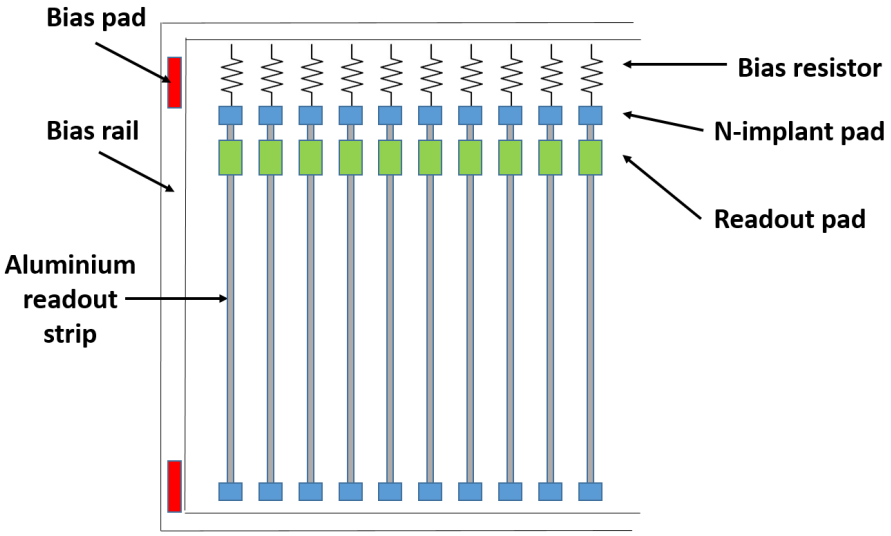

Figure 4. Schematic layout of the strip sensor design highlighting the key structures used for testing.

A full set of 45 XY and 45 UV sensors have been delivered by Hamamatsu Photonics U.K. These sensors have all been tested to ensure they complied with the specifications given and that they are fit for purpose. Figure 4 shows a schematic of the sensor layout highlighting the key structures used during testing.

An initial set of reception tests were performed on every device to ensure they were functional and undamaged. These tests consisted of a visual inspection of each sensor to check for obvious damage or defects followed by an IV sweep to measure the total leakage current. A Keithley 2470 source meter was used to provide a bias between the bias rail and the back plane of the device. A bias of 0 to 120 V was applied in 2 V steps with a wait of 5 s between performing the step and measuring the resulting current. After reaching 120 V the voltage was then fixed and the current was measured every 10 s for 10 minutes to ensure there was no drift in the current over time. The conditions throughout the test were 22°, 40% humidity. The results of the ramping phase are shown in figure 5. The target performance for all devices was $< 0.1\,\mu A/cm^2$ at full depletion (~ 100 V) and was met by all sensors, however 3 of the sensors showed signs of breakdown occurring at higher voltages and so will be excluded from use in the final system. In all cases except these 3 devices it was found that the current remained steady during the 10 minute stability test.

As well as the reception testing a suite of tests were performed to characterise the sensors and ensure that all the relevant specifications had been met. These tests were carried out on a small random sub-sample of the sensors as they are expected to be common across all sensors. A full summary of all the device specifications and the results of the measurements to check them are given in table 3.

A key parameter of interest was the total load capacitance of each channel as this will strongly impact the noise levels of the system. This total load represents the sum of the strip to back plane capacitance, inter-strip capacitance and additional contributions from the second metal layer on the

2023 JINST 18 P04026

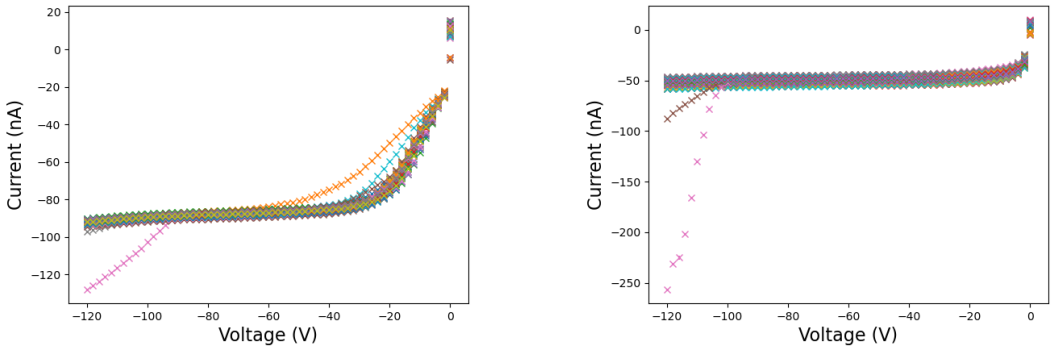

Figure 5. Measurements of the leakage current on the XY (left) and UV (right) for all 45 sensors of each type. Each colour represents a different sensor.

Table 3. Comparison of the specifications and measured properties of the silicon sensors. Properties in which the devices significantly surpassed the required performance are shown in bold.

Property	Specification UV(XY)	Measured Value UV(XY)
Wafer substrate	p-type float-zone	
Depletion voltage (V)	<100	92
Maximum operating voltage (V)	**150**	**> 600**
Leakage Current at full depletion ($\mu A/cm^2$)	**< 0.1**	**0.001**
Load capacitance per channel (pF)	**< 22**	**13 (10–19)**
Inter-strip resistance (MΩ)	> 10	> 10
Bias Resistor (MΩ)	1.5 ± 0.5	1.53 ± 0.07
Channel failure rate	**< 2%**	**< 0.01%**
Dimensions		
Width (mm)	59.1 (120.0)	
Height (mm)	60.0 (60.0)	
Sensor Thickness (µm)	150.0	
Strip pitch (µm)	159 (232)	

Y strips, and was specified to be < 22 pF at full depletion. The total strip to back plane capacitance was measured using a Wayne-Kerr 6500b LCR meter with a 10 kHz AC signal with amplitude 500 mV while biasing the sensor between the back plane and the bias rail using the Keithley 2470. The measurement was performed over the range 0 to 150 V in 2 V steps with 5 s rests between steps and measurements. The results from this measurement are shown in figure 6. The capacitance per strip was then calculated by simply dividing the measured value by the number of strips on the sensor. This measurement also allowed the extraction of the depletion voltage of the sensors which was found to be 92 V.

The inter-strip capacitance was slightly more complicated to measure. Throughout this measurement the sensor was biased to 120 V as described above to ensure the sensor was fully depleted. The LCR meter was then connected to the readout pads of 2 adjacent strips and operated at

2023 JINST 18 P04026

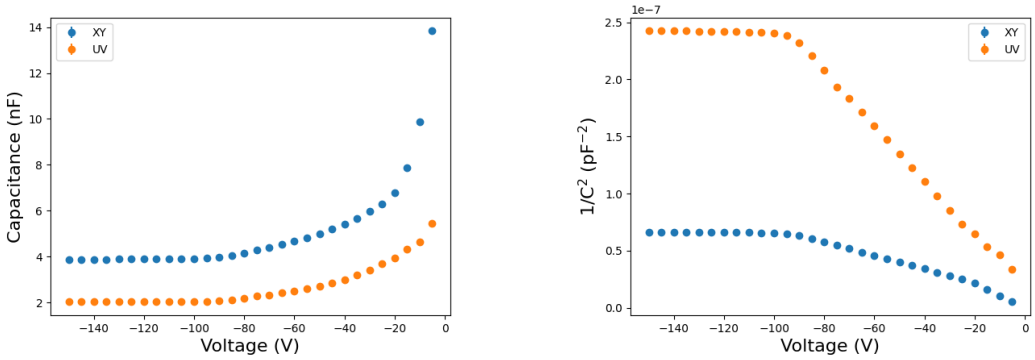

Figure 6. Measurements of the capacitance between the bias rail and back plane as a function of voltage for a single XY and UV sensor. Each XY sensor is approximately twice the area of a UV sensor.

100 kHz, 500 mV. In order to measure the contribution not just from the nearest neighbour, but from both neighbours and the next to nearest neighbours it is necessary to couple all the neighbouring pads so that they can be held at the same voltage. Due to limitations on the number of probes available this was achieved by wire bonding between the readout pads of the neighbouring pads to achieve the configuration shown in figure 7 (left). In practice this measurement was done in stages, initially with no bond in place, then a single bond between the nearest neighbours, then the full bonding setup between both nearest neighbours and next to nearest neighbours. The resulting capacitances measured for the X strips were 1 pF, 2 pF and 2.2 pF respectively indicating that the contributions from the next to nearest neighbours was only 10% of that from the nearest neighbours indicating that more distant neighbours can be ignored. In the case of the Y strips the situation is complicated further as the second layer of metal for redirecting the signal runs perpendicular to the first metal layer and as such there is a potential coupling between all the strips. As such it was necessary to bond between every channel except that being tested such that the contributions from all neighbours could be measured. This is shown in figure 7 (right). For the Y strips the inter-strip capacitance will vary based on the position of the channel as the length of the second metal layer changes across the sensor. To ensure the worst case scenario was measured, the measurement was performed on a channel at the end which has the longest second metal section. The results of measuring all these various capacitances are summarised in table 4.

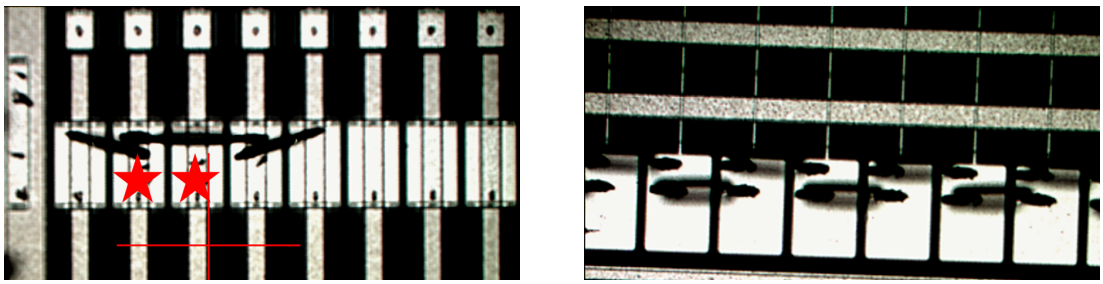

Figure 7. Examples of the wire bonding used for measuring inter-strip capacitance. Left shows the setup for an X, U or V type strip with the probe contact points indicated by stars. The right shows a segment of the y sensor where all channels have been bonded together.

2023 JINST 18 P04026

Table 4. Breakdown of the measured capacitance for each sensor type.

Sensor	Strip to Back Plane (pF)	Interstrip (pF)	Total (pF)
UV	8.0	5.0	13.0
X	7.6	2.3	9.9
Y	7.6	11.8	19.4

Further to the capacitance a variety of key resistances were measured using simple IV scans and extracting the gradient. First the bias resistor was tested by probing between the bias rail and N-implant pad at the resistor end of the strip and was found to have a value 1.53 MΩ ± 0.07 MΩ which meets the specification of 1.5 MΩ ± 0.5 MΩ. The N-implant resistance was then measured by measuring the difference in resistance when biasing between 2 adjacent N-implant pads of a UV sensor at the bias resistor end and then at the opposite end. The measured resistances were 2.96 MΩ and 3.06 MΩ indicating a resistance of ~6 MΩ/cm which meets the specification of < 20 MΩ/cm. From the fact that the resistance between adjacent N-implant pads is approximately twice that of the bias resistor it can also be further inferred that the criteria of the interstrip resistance being > 10 MΩ has also been met.

A final test was performed to check for coupling shorts on each strip by applying 5 V between the N-implant pad and the readout pad. This was performed on every strip for 2 randomly selected sensors and the results were found to agree with Hamamatsu's internal testing which suggested a strip failure rate of 1/30000 strips.

Further to sensor testing, work has been carried out to develop a reliable assembly procedure for gluing and aligning the sensors on the sensor boards. Using a prototype of the sensor board it was found that using CW2400 conductive adhesive with a manual pick and place machine and suitable fiducial markers, it was possible to achieve an accuracy of better than 50 µm on the position of the sensor with rotations of < 0.01°. An example of a successful attempt at assembling a full XY sensor board with three XY sensors tiled together is shown in figure 8, while an image of the corners of two UV sensors that have been successfully aligned to a 100 µm wide fiducial marker is shown in figure 9. The leakage current measurement was repeated on each sensor after gluing to ensure the sensor was undamaged by the assembly procedure and no issues were found for any sensors.

Figure 8. First attempt at assembling an XY sensor board with three tiled XY sensors.

3 Simulation

To optimize the design and evaluate the performance of the system, detailed simulations of the detectors and their interaction with a proton beam were modelled in Geant4 v10.0.4 [12, 13] using the QGSP_BIC_EMY physics list. The detector model is shown in figure 10.

2023 JINST 18 P04026

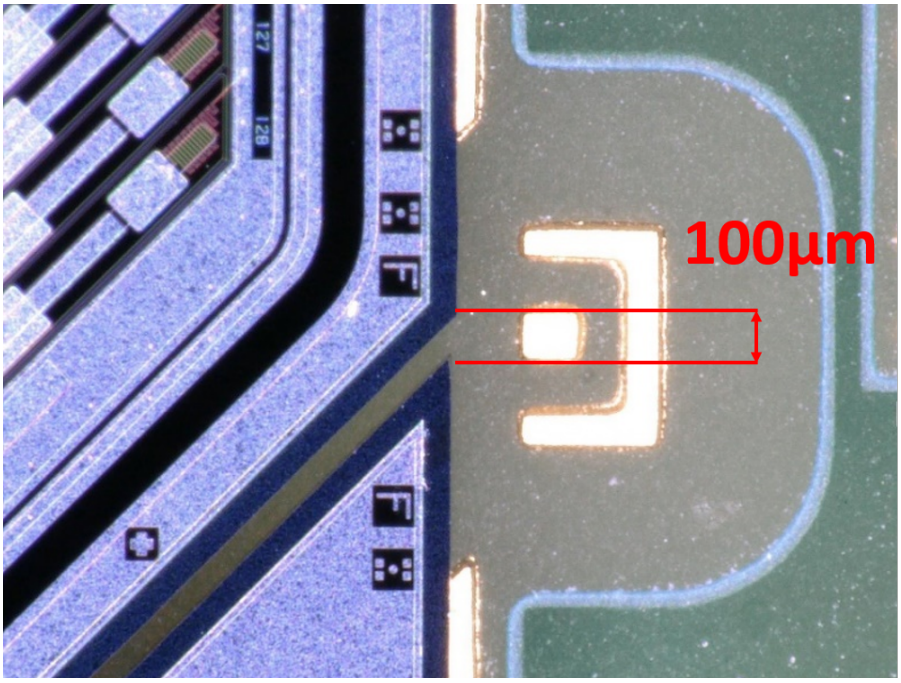

Figure 9. An example of the alignment between two U/V sensors using a 100 µm wide fiducial marker when glued to a sensor board.

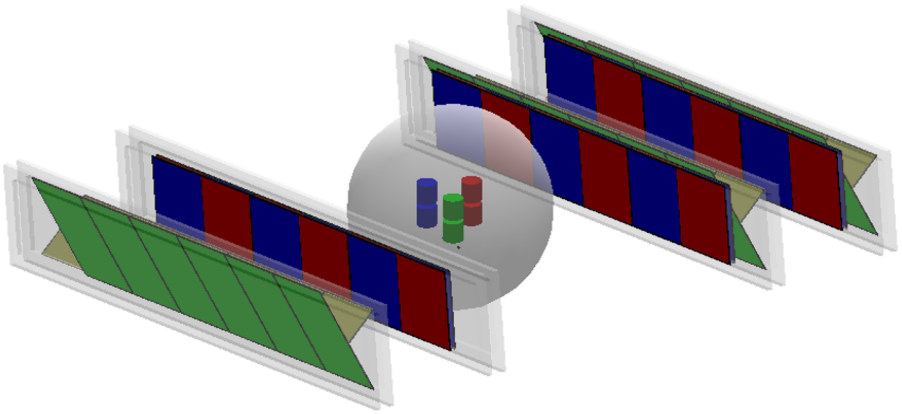

Figure 10. Geant4 model of the OPTIma system showing the mounted X (red), Y (blue), U (green) and V (yellow) strip sensors along with the inactive regions of each device (black). An example 150 mm diameter bauble phantom containing 6 inserts also included.

3.1 Detector

The simulated detector matches that described in section 2. Each silicon sensor is modelled as a discrete object with a ~ 550 µm region of dead silicon at each edge, and a gap of 100 µm is placed between sensors to account for realistic alignment procedures. Each sensor is treated as having 100% charge collection efficiency, however charge diffusion is included to account for charge being shared across strips. The charge spatial distribution is assumed to follow a Gaussian distribution

2023 JINST 18 P04026

about the hit position with width given by eq. (3.1)[14].

$$\sigma = \sqrt{\frac{2kTd^2}{eV_b}} \tag{3.1}$$

Where k is the Boltzmann constant, T is temperature, d is detector thickness, e is elementary charge, and V_b is the bias voltage of the sensor (120 V). A randomly generated noise is also generated for each strip based on an expected noise of 1500 (2000) electrons for each X, U, V (Y) type strip. These values are based on the experimentally measured load capacitance for each channel along with the preliminary ASIC design. Following charge diffusion and noise generation, a threshold of 10,000 e is applied to each strip to remove the noise, and the address of any strip above threshold is recorded for use in track reconstruction.

3.2 Beam model

The beam was modelled using a parameterization of the research beamline at The Christie. A 230 MeV beam was chosen to allow for penetration of up to 220 mm of water while still yielding a reasonable residual energy [15], with an expected beam energy spread of $\sigma = 1$ MeV. A total spot width of 40 mm (Gaussian with $\sigma = 10$ mm) was used based on trials performed by the Christie team to find the maximum scannable beam size. This relatively large beam size is desirable as a larger spatial separation of the protons reduces the number of ambiguities during track reconstruction.

To reduce the number of simulations required, it was assumed that there was exactly one proton per bunch/readout window during the simulation stage. To recreate realistic beam currents, the output of these single proton simulations were then merged to produce multi-proton events where the number of protons per bunch is expected to follow a Poisson distribution with a mean set by the beam current. As the strip readout will be binary, if more than one proton generated a hit in the same channel, that channel was only recorded once in the merged output. The merging was performed after the threshold had been applied to each channel. As such, it neglects cases where the charge produced by individual protons in a particular channel is below threshold but their combined charge would be above threshold. This represents a slight underestimate of the true detector efficiency, however such cases are rare and will not have a significant impact on the results shown here.

3.3 Phantom

The phantom used for benchmarking the detector performance is a variation of the bauble phantom used by PRaVDA [9]. Here the phantom has been scaled up to a total diameter of 150 mm by adding extra Perspex to give a diameter similar to that of a pediatric head. The phantom is embedded with 6 cylindrical inserts of length 15 mm and diameter 15 mm, made of tissue equivalent materials, with properties given in table 5. The inserts are grouped into 2 layers- 3 high contrast materials, 3 low contrast- with the 2 sets of inserts positioned at a y position of +10 mm and −10 mm respectively. Within each group the 3 inserts are equidistant from each other and are positioned at a radius of 19 mm in the x-z plane, where z is the beam axis and y is the axis along which the detectors are translated. For clarity 2 projections of the phantom are shown in figure 11.

2023 JINST 18 P04026

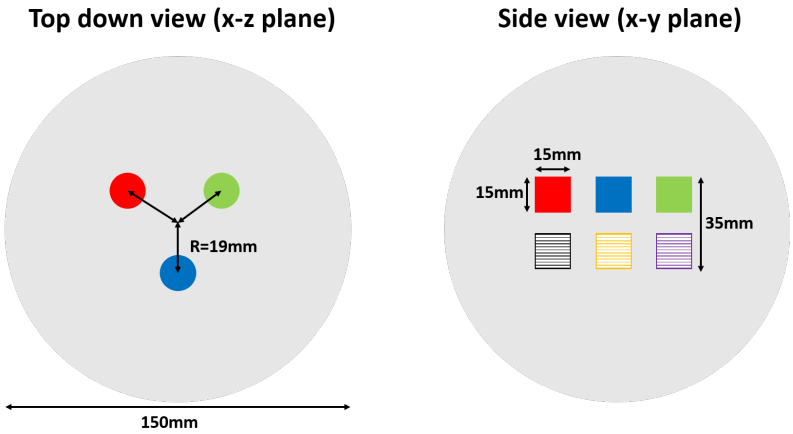

Figure 11. Layout of the bauble phantom, a 150 mm Perspex sphere containing 3 high contrast (solid) and 3 low contrast (striped) tissue equivalent inserts used for benchmarking performance. The materials used for the inserts are cortical bone (red), air (green), lung (blue), rib bone (black), adipose (orange) and water (purple).

Table 5. Materials used as inserts in the bauble phantom.

Material	RSP	Contrast	Density (g/cm^3)
Perspex	1.16	–	1.18
Cortical Bone	1.64	High	1.84
Lung	0.29	High	0.30
Air	0.00	High	0.00
Rib Bone	1.32	Low	1.40
Water	0.99	Low	1.00
Adipose	0.91	Low	0.92

3.4 Scan procedure

As the active area of each module is only 60 mm high, it is necessary to translate the detector to cover a full scan area of $\sim 360 \times 360\,\text{mm}^2$. This will be done by scanning the beam horizontally, stopping the beam, translating the sensor vertically in steps matching the beam size, then repeating until the full area is covered. In order to avoid producing artefacts in the images due to the dead areas from tiling the XY sensors, a small skew of 6° is introduced to the detector so that the gaps in coverage in each horizontal scan are not aligned with those in the next step and so full coverage is obtained by summing across all horizontal scans. Once the full scan area has been covered the detectors are then rotated around the phantom in 1° steps until 360 projections have been acquired.

In practice when developing the system it will not be possible to mount the system on a gantry and so it will not be possible to translate the detectors. Instead the vertical translations and rotations will be simulated by moving the phantom instead of the detector.

When simulating, each continuous horizontal scan is approximated by a horizontal series of spots separated by the spot width. Such an approximation leads to a uniform dose distribution over the full scan area while ensuring that the spatial distribution of the protons within each bunch remains realistic.

2023 JINST 18 P04026

4 Track reconstruction

Track reconstruction was performed using a dedicated C++ package, OPERA++, which proceeds in three main steps.

Firstly, proton hit locations are reconstructed within each module. For each sensor board, candidate hit locations are reconstructed by finding all possible intersections of strips above threshold from the pair of layers. As there is only one sensor board in the front two modules, no further reduction of ambiguities can be performed and so the number of hits will go as the square of the number of protons within the bunch. In the rear modules the position of these candidate hits is compared across the two sets of sensor boards, and any pair of candidates with a radial separation (relative to the beam axis) less than a value of R_1 is recorded.

Secondly, "mini-tracks" are formed in both pairs of trackers. In the upstream pair of trackers, as the beam is travelling through minimal material, it can be assumed that the protons travel in an approximately straight line parallel to the beam axis. As such, mini-tracks are formed by finding the pair of hits from each module that have the smallest radial separation (relative to the beam axis), removing these hits, then repeating until a maximum of N mini-tracks are produced, where N is the number of protons within the bunch. N is estimated for each bunch by calculating the median number of strips above threshold in each layer of the upstream trackers. Using the median rather than mean number of strips was found to give the best performance by minimising contributions from strip noise or inefficiencies. An additional cut, R_2, is placed on the radial separation value for each mini-track to remove any mini-tracks that are not found to be parallel with the expected beam axis. In the downstream trackers no limit is placed on the number of mini-tracks that can be formed as the correlation between the proton path and the incoming beam axis is not as strong due to scattering in the patient/phantom, however a loose cut on the maximum separation, R_3, of each pair of hits (relative to the nominal beam axis) is still imposed to remove candidate tracks that would correspond to unexpectedly large amounts of scattering.

Lastly, the final set of tracks is found by taking each upstream mini-track and finding the downstream mini-track that is closest to it when both tracks are projected to a plane at z=0 (the centre of the phantom). Again, a cut on this separation, R_4 is imposed to remove any cases in which the chances of the 2 tracks corresponding to 1 proton are unlikely for the amount of scattering expected.

The values $R_{1...4}$ are all tunable parameters that will impact the balance between efficiency and purity of the track finding. Currently these values are all chosen by simulating a set of single protons through a block of Perspex with a thickness equivalent to the maximum thickness of the target phantom, measuring the relevant radial separation parameters, and setting the values of $R_{1...4}$ to 3× the mean values recorded for single protons. While crude, this approach is found to yield high tracking efficiency and purity (> 80% and > 90% respectively) for low currents and can be easily adapted to an experimentally driven calibration in which these parameters are directly measured using any bunches containing just one proton. Here efficiency is defined as the fraction of true proton trajectories that are successfully reconstructed, while purity is defined as the fraction of reconstructed tracks which can be matched to a true proton path. For higher currents it may be desirable to tighten these cuts so as to recover the purity in high multiplicity bunches, though this would come at the cost of tracking efficiency.

2023 JINST 18 P04026

In future, each track would then be associated to a hit within a calorimeter in order to determine the residual energy of each proton, however the calorimeter is not currently included within the Geant4 model. For now, the true energy of each proton is simply recorded then smeared according to the expected single proton performance of the ASTRA calorimeter [11] before associating it with each track. Path dependent corrections are then applied to the nominal beam energy and the recorded residual energy to account for energy losses within the detector and air so that an accurate estimate of the energy at the point of entry and exit to the phantom can be determined.

It is likely that further improvements to efficiency and purity could be achieved by switching from this piecewise approach to one that performs a fitting across all 12 silicon layers at once, however due to the complicated combinatorics that arise and the large number of protons required to produce an image of suitable quality, the piecewise approach is currently preferred for minimising reconstruction times.

5 Performance

To determine the performance of the system, a simulated pCT was performed on the phantom using 360 projections following the procedure described in section 3.4. A total of $\sim 10^7$ protons were simulated per projection with each projection covering an area of $200 \times 200\,\mathrm{mm}^2$. The reconstructed proton tracks were then passed through a backprojection-then-filtering based algorithm [16] to produce a 3D map of the RSP using 1 mm^3 voxels. Initially it was found that simply running the raw projections through the image reconstruction algorithm produced some artefacts in the images due to the fact the beam angle varies within each projection when using a scanned pencil beam, however it was found that simply re-binning the proton trajectories into the projection in which they are closest to parallel was sufficient for removing these artefacts. A slice of the resulting images showing the high contrast inserts is shown in figure 12.

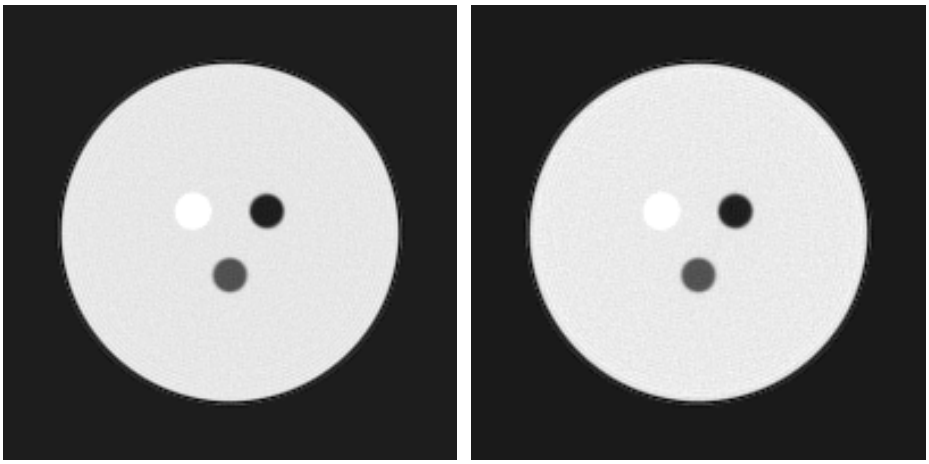

(a) 10 pA (b) 50 pA

Figure 12. A slice through the high contrast inserts (top left: Cortical Bone, top right:Air, bottom: Lung) for images generated using 10 and 50 pA beam currents.

2023 JINST 18 P04026

The performance of the detector was evaluated by measuring the mean RSP within the central region ($r < 8$ mm) of each insert and comparing it to the "true" RSP as a function of beam current. The figure of merit chosen was the RSP discrepancy which is defined as:

$$\text{RSP Discrepancy} = \frac{\text{RSP}_{\text{Measured}} - \text{RSP}_{\text{True}}}{\text{RSP}_{\text{True}}} \tag{5.1}$$

Where the "true" RSP was determined by performing a simulated pCT of the phantom with no detectors in place, extracting the true proton trajectories and energies from the simulation, then running these trajectories through the same image reconstruction algorithm. This approach was chosen to factor out any potential issues with the reconstruction algorithm, however in practice this was not strictly necessary as it was found to yield results in agreement with those seen from simulating simple water tank style experiments.

The resulting RSP discrepancy as a function of material and current is shown in figure 13 along with the expected performance if all bunches contained only single protons. In all cases the total integrated dose has been kept constant to allow for fair comparison, though it should be noted that the fraction of this fixed dose which is successfully reconstructed will vary with current.

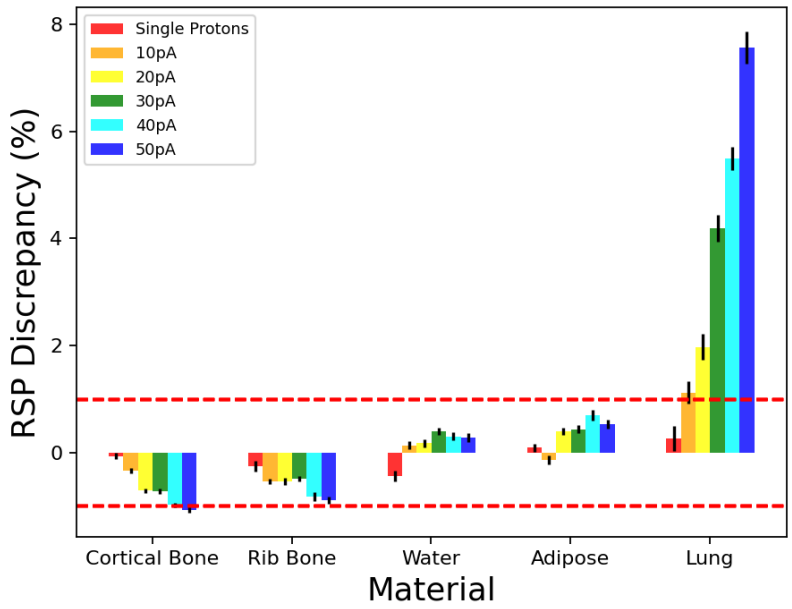

Figure 13. Fractional difference between the mean reconstructed RSP and the true value for each insert as a function of beam current. The single proton result indicates the performance when tracking ambiguities are removed. The dashed red line shows the target performance of 1%.

The results show that the performance is material and current dependent but that a discrepancy of $< 1\%$ can be achieved in many of the materials even up to currents of 50 pA, with the best performance seen for lower currents and materials with an RSP similar to that of the surrounding Perspex.

The dependence of the performance on current is a result of tracking ambiguities. As the current increases, so will the number of protons per bunch. The reconstruction algorithm tries to assign

2023 JINST 18 P04026

hits into separate tracks by assuming the most likely path for a proton is a straight line parallel to the beam axis, however as more hits are introduced, the likelihood of a random assortment of hits coincidentally producing a straighter track than any of the real proton paths increases and so the reconstruction becomes more likely to return incorrect proton trajectories. As all the hits within a bunch are inherently bound to lie within the beam area, the trajectory of these incorrect tracks will always lie within a beam width of the true trajectory. The net impact of this is that the RSP measured for any voxel will be the average of the true RSP of that voxel and the RSP of the neighbouring voxels, where the weighting of this averaging is determined by the rate of track misreconstruction. This results in a blurring of the images which can be seen by looking at a line profile through the cortical bone and air inserts (figure 14) which shows that as the beam current increases, the RSP measured within each insert is increasingly biased towards the RSP of the surrounding Perspex.

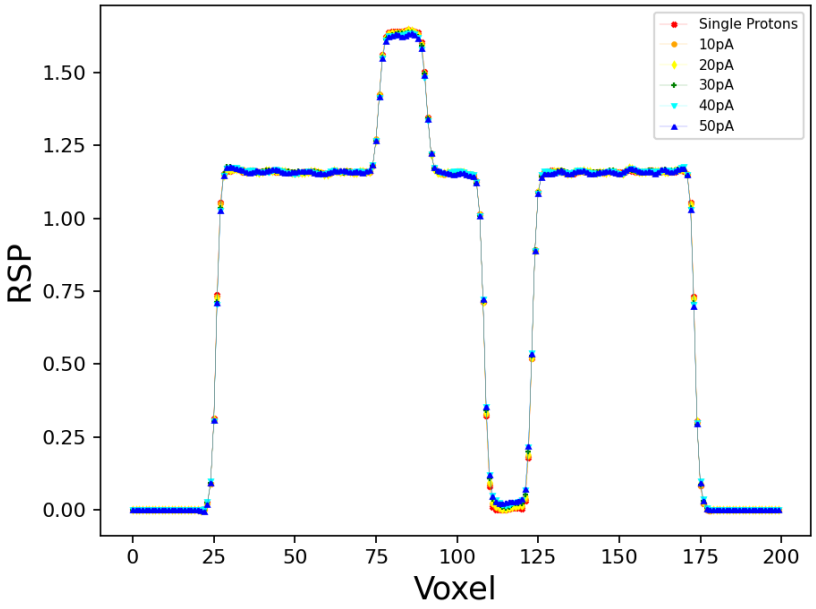

Figure 14. A line profile through the cortical bone and air inserts. As the beam current increases it is observed that the RSP measured for each insert is increasingly biased towards the RSP of the surrounding Perspex.

This also explains the material dependence in figure 13. As the bulk of the material is made of Perspex, the effect of the blurring acts to push the recorded RSP towards that of Perspex, hence it is observed that materials with an RSP higher than that of Perspex display a negative bias while those with lower RSPs see a positive bias. For materials with an RSP very similar to that of Perspex, the fractional change in RSP is less significant than it is for those with a much higher contrast such as lung. There will also be a contribution from the energy dependence of the calorimeter performance which gives a better resolution for higher residual energies, however given the strong dependence on current, this is assumed to be a secondary effect.

Due to the nature of this blurring, care must be taken when trying to directly relate these results to a treatment planning scenario. Here a phantom that is mostly made of a single bulk material that

2023 JINST 18 P04026

contains small inserts with vastly different RSPs has been chosen. If a different bulk material was chosen or the inserts were a different size, the results may have been quite different, e.g. if the bulk had a much lower RSP, then the lung discrepancy would improve while the cortical bone would worsen, or if the inserts were much larger then all materials would show an improvement in their discrepancy. However, it should be noted that the small, high contrast objects shown here represent a particularly challenging scenario compared to typical anatomical features which can be more homogeneous, and so the ability to achieve better than 1% discrepancy for a wide range of materials at these currents suggests a good performance might be achieved in anthropomorphic phantoms too.

Additionally, while the results from figure 13 highlight the performance in terms of raw RSP discrepancy, it is worth noting that the more relevant parameter of interest for treatment planning is the accuracy of the integrated RSP along a particular path as this is what impacts the range uncertainty and thus determines the required safety margins in any treatment plan.

While these two quantities are linked, it is not trivial to extrapolate these results to the impact they would have on treatment planning, particularly as any bias in the observed RSP caused by blurring would be expected to be correlated with the bias in neighbouring tissues e.g. at a boundary between a low and a high RSP material, blurring will result in a positive bias of the RSP measured in the low material and a negative bias in the RSP measured in the high material. Ultimately, further studies using anthropomorphic phantoms with realistic RSP profiles must be carried out before any final conclusions can be made about the performance of high current pCT in clinical applications.

6 Outlook & discussion

Here we have presented a solution for tracking in a high current environment, however this only solves half the problem of pCT. To construct a full system it will also be necessary to produce a system for measuring the residual proton energy in such an environment. Many solutions have been proposed based on range telescopes, calorimeters and time of flight measurements [9, 11, 17, 18], however they typically are limited by at least one of cost, size or speed. OPTIma will be pursuing a compact segmented calorimeter approach based on scintillating bars, however the optimal solution for this problem is still an open challenge for the field.

In terms of tracking performance the solution presented here represents a considerable step towards operating at clinical treatment currents however it is unlikely that a strip based approach can be pushed much further as ambiguities can only be reduced by adding more layers and thus putting more material in the beam which compromises the energy measurement. A pixel based solution represents one potential improvement as a single layer provides the required (x,y) position of the proton meaning there are no ambiguities at a module level and more modules can be used for track disambiguation without adding more material to the beam. However, such a solution requires many more channels so a suitable high-speed data driven read-out needs to be implemented and issues of power dissipation may become more complex. Such a solution is also ultimately still limited by the ability to match tracks from before and after the patient that have undergone scattering. Iterative based reconstruction approaches might help improve this by providing an initial image reconstruction to roughly map out the RSP, then using this information to inform the next iteration of track reconstruction on what is a likely amount of scattering for a particular trajectory, however this is still a novel idea for pCT.

2023 JINST 18 P04026

Lastly, while the blurring effect of ambiguities effectively results in a degradation of the spatial resolution of the image, it is worth noting that patients are likely to have already had more than one type of scan performed on them by the time they would receive pCT. As such, it is possible that information from a higher spatial resolution image such as an xCT or MRI might be combined with pCT to further improve treatment planning. Such approaches are already becoming common in conventional radiotherapy treatment planning where MRIs are used to improve soft tissue contrast [19].

7 Conclusion

The design for a new set of silicon strip based trackers currently under construction by OPTIma has been presented along with details on how such a system can be used to perform pCT in high-current environments in order to reduce the gap between the currents required for imaging and treatment. The sensors required for the system have been delivered and tested and a suitable assembly procedure has been developed for aligning sensors with an accuracy of $< 50\mu$m. Detailed Geant4 based simulations were used to evaluate the performance of the device when used at a clinical treatment facility using a high current, spot scanning beam, and showed that a performance of $< 1\%$ discrepancy on the RSP could be achieved for various materials embedded in 150 mm of Perspex at currents in the range 10–50 pA. By accepting up to 7 protons per bunch, it was shown that pct can be performed at beam currents 5 times greater than those required for single proton systems, thus reducing the gap between the beam currents required for pCT and those used for treatment, while also significantly reducing the beam time required for producing an image. Validation of these studies will be performed in future using an anthropomorphic head phantom at The Christie Proton Beam Therapy Centre, Manchester.

Acknowledgments

This work was supported by EPSRC under the grant EP/R023220/1.

References

[1] B. Li, H.C. Lee, X. Duan, C. Shen, L. Zhou, X. Jia et al., *Comprehensive analysis of proton range uncertainties related to stopping-power-ratio estimation using dual-energy CT imaging*, *Phys. Med. Biol.* **62** (2017) 7056.

[2] N. Peters, P. Wohlfahrt, C. Hofmann, C. MÃ¶hler, S. Menkel, M. Tschiche et al., *Reduction of clinical safety margins in proton therapy enabled by the clinical implementation of dual-energy CT for direct stopping-power prediction*, *Radiother. Oncol.* **166** (2022) 71.

[3] R.W. Schulte and S.N. Penfold, *Proton CT for Improved Stopping Power Determination in Proton Therapy*, *Trans. Am. Nucl. Soc* **106** (2012) 55.

[4] H.F.W. Sadrozinski, R.P. Johnson, S. Macafee, A. Plumb, D. Steinberg, A. Zatserklyaniy et al., *Development of a head scanner for proton CT*, *Nucl. Instrum. Meth. A* **699** (2013) 205.

[5] R.P. Johnson, *Review of medical radiography and tomography with proton beams*, *Rep. Prog. Phys.* **81** (2018) 016701.

2023 JINST 18 P04026

[6] H. Owen, D. Holder, J. Alonso and R. MacKay, *Technologies for Delivery of Proton and Ion Beams for Radiotherapy*, *Int. J. Mod. Phys. A* **29** (2014) 1441002 [arXiv:1310.0237].

[7] M. Durante and H. Paganetti, *Nuclear physics in particle therapy: a review*, *Rep. Prog. Phys.* **79** (2016) 096702.

[8] N.G. Burnet, R.I. Mackay, E. Smith, A.L. Chadwick, G.A. Whitfield, D.J. Thomson et al., *Proton beam therapy: perspectives on the national health service england clinical service and research programme*, *Br. J. Radiol.* **93** (2020) 20190873.

[9] M. Esposito, C. Waltham, J.T. Taylor, S. Manger, B. Phoenix, T. Price et al., *PRaVDA: The first solid-state system for proton computed tomography*, *Phys. Med.* **55** (2018) 149.

[10] ATLAS collaboration, *Technical Design Report for the ATLAS Inner Tracker Strip Detector*, Tech. Rep., CERN-LHCC-2017-005 (2017).

[11] M. Granado-González, C. Jesús-Valls, T. Lux, T. Price and F. Sánchez, *A novel range telescope concept for proton CT*, *Phys. Med. Biol.* **67** (2022) 035013 [arXiv:2109.03452].

[12] GEANT4 collaboration, *GEANT4–a simulation toolkit*, *Nucl. Instrum. Meth. A* **506** (2003) 250.

[13] J. Allison et al., *Recent developments in Geant4*, *Nucl. Instrum. Meth. A* **835** (2016) 186.

[14] H.W. Kraner, R. Beuttenmuller, T. Ludlam, A.L. Hanson, K.W. Jones, V. Radeka et al., *CHARGE COLLECTION IN SILICON STRIP DETECTORS. (TALK)*, *IEEE Trans. Nucl. Sci.* **30** (1983) 405.

[15] A.T. Herrod, A. Winter, S. Psoroulas, T. Price, H.L. Owen, R.B. Appleby et al., *Optimal Configuration of Proton-Therapy Accelerators for Relative-Stopping-Power Resolution in Proton Computed Tomography*, *Phys. Rev. Appl.* **18** (2022) 014020 [arXiv:2111.02712].

[16] G. Poludniowski, N.M. Allinson and P.M. Evans, *Proton computed tomography reconstruction using a backprojection-then-filtering approach*, *Phys. Med. Biol.* **59** (2014) 7905.

[17] S. Mattiazzo et al., *iMPACT: An Innovative Tracker and Calorimeter for Proton Computed Tomography*, *IEEE Trans. Radiat. Plasma Med. Sci.* **2** (2018) 345.

[18] F. Ulrich-Pur, T. Bergauer, A. Burker, A. Hirtl, C. Irmler, S. Kaser et al., *Feasibility study of a proton CT system based on 4d-tracking and residual energy determination via time-of-flight*, *Phys. Med. Biol.* **67** (2022) 095005.

[19] M.A. Schmidt and G.S. Payne, *Radiotherapy planning using MRI*, *Phys. Med. Biol.* **60** (2015) R323.

2023 JINST 18 P04026